arXiv:1610.07196v1 [cond-mat.mes-hall] 23 Oct 2016

Graphene-WS_2 heterostructures for tunable spin injection and spin transport

S. Omar[1,*] and B.J. van Wees[1]

[1] *The Zernike Institute for Advanced Materials University of Groningen Nijenborgh 4 9747 AG, Groningen, The Netherlands*

(Dated: October 25, 2016)

We report the first measurements of spin injection in to graphene through a 20 nm thick tungsten disulphide (WS_2) layer, along with a modified spin relaxation time (τ_s) in graphene in the WS_2 environment, via spin-valve and Hanle spin-precession measurements, respectively. First, during the spin-injection into graphene through a WS_2-graphene interface, we can tune the interface resistance at different current bias and modify the spin injection efficiency, in a correlation with the conductivity-mismatch theory. Temperature assisted tunneling is identified as a dominant mechanism for the charge transport across the interface. Second, we measure the spin transport in graphene, underneath the WS_2 crystal and observe a significant reduction in the τ_s down to 17 ps in graphene in the WS_2 covered region, compared to that in its pristine state. The reduced τ_s indicates the WS_2-proximity induced additional dephasing of the spins in graphene.

PACS numbers: 85.75.-d, 73.22.Pr, 75.76.j

Keywords: Spintronics, Graphene, spin injection, tunnel barrier, Schottky barrier, graphene-semiconductor interface, thermally assisted tunneling

Graphene, an ideal material for spin transport due to low spin-orbit coupling and small hyperfine interactions [1, 2], has shown a significant improvement in its spin transport properties over the years [3, 4]. However, tuning of the spin injection and transport properties remains illusive for graphene, inhibiting the demonstration of graphene as a spin-transistor [5]. There is also a rapidly growing interest in other layered two-dimensional materials such as transition metal dichalcogenides (TMDs) due to their novel properties such as presence of band-gap accompanied by a significant spin orbit coupling up to few hundreds of meV, which is lacking in graphene [6–10]. In the absence of an inversion center in the lattice, these materials with an odd number of layers also provide access to the novel physical phenomena related to the valley coupled spin degree of freedom of the charge carriers [11–13], which adds extra functionality to these materials. A combination of graphene with these 2-D materials appears to be a plausible option to overcome the aforementioned shortcomings.

In recent years, there have been a lot of studies on graphene-2-D material heterostructures demonstrating novel charge transport properties across the interface [14–17]. The 2-D materials such as hexagonal boron nitride (h-BN) can be used in spintronic devices as tunnel barriers for spin injection in graphene, replacing the conventional oxide tunnel barriers [18–20]. In contrast to an insulating tunnel barrier, the use of band-gap 2-D semiconductors such as TMDs (i.e. MoS_2, WS_2) during spin-injection, can lead to attractive features such as tuning of the interface resistance along with the induced spin orbit coupling at the graphene-TMD interface [21–26], which in turn can modulate the spin-injection efficiency as well as the spin transport properties in graphene. Recently reported weak localization [27], Shubnikov-de Haas magnetoresistance measurements [25] and spin-Hall experiments [28] on graphene-WS_2 (Gr-WS_2) heterostructures reveal that the spin-lifetime (τ_s) in graphene is greatly reduced from nanoseconds to picoseconds due to significantly induced spin-orbit coupling ($\sim$ 5-15 meV) in graphene. However, spin transport experiments on this system would provide a more convincing proof of this phenomenon.

We report the first measurements of spin injection in to graphene through a 20 nm thick WS_2 layer, along with a reduced spin relaxation time in graphene in the WS_2 environment, via Hanle spin-precession measurements. By applying a voltage bias between graphene and the semiconducting TMD layer, we tune the interface resistance and modify the spin injection efficiency. We measure a higher spin signal for a higher interface resistance at the injector. In this way spins cannot flow back and get relaxed at the interface or in the bulk WS_2, suppressing the contact induced spin relaxation. We also perform temperature dependent measurements for a Gr-WS_2 heterostructure and find that the ideality factor, which is a measure of thermionic emission of the charge carriers across a potential energy barrier, is much greater than one. It indicates that there are other transport mechanisms such as temperature or field assisted tunneling across the interface, contributing to the spin injection process in graphene. We also measure the spin transport in graphene underneath the WS_2 crystal, where we inject and detect the spin accumulation in graphene using the ferromagnetic tunneling contacts. We observe a significant reduction in τ_s, when the spins travel across the WS_2 encapsulated region, compared to τ_s obtained for the non-encapsulated region. The reduced τ_s suggests towards an induced spin-orbit coupling/ spin absorption at the Gr-WS_2 interface.

We prepare graphene-WS_2 heterostructures via a pick up transfer method, described in ref. [29] (see supple-

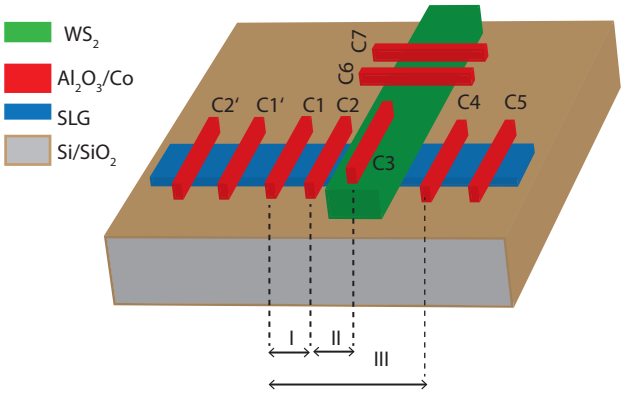

FIG. 1. A schematic of graphene-WS_2 heterostructure with ferromagnetic contacts with Al_2O_3 tunnel barriers between cobalt and graphene(WS_2). The regions labeled as I, II and III are 2.0 μm, 2.5 μm and 6.5 μm long, respectively. The WS_2 covered region is $\sim$ 3.0 μm.

mentary for details) using a single layer graphene and a thick WS_2 flake, obtained via scotch tape exfoliation procedure. This dry transfer method enables the formation of a clean and chemical free Gr-WS_2 interface, which has been reported to have less impurities and superior charge transport properties [30] compared to the stacks prepared via CVD grown 2-D materials [14]. Moreover, we transfer a thick WS_2 flake on to graphene, in order to reduce the bubble formation during the transfer process [31]. The ferromagnetic (FM) contacts are patterned both on graphene and on WS_2 via electron beam lithography on the PMMA (poly (methyl methacrylate)) coated Gr-WS_2 stack. Then, 0.6 nm of aluminum (Al) is deposited in two steps, each step of 0.3 nm of Al deposition followed by in-situ oxidation by pure O_2 to form an oxide tunnel barrier to overcome the conductivity mismatch problem [32]. On top of the oxide barrier we deposit 55 nm of cobalt for the spin polarized contacts. To prevent the oxidation of the ferromagnetic electrodes, the contacts are covered with 3 nm thick aluminum layer.

We characterize the charge and spin transport in graphene at three different regimes, labeled as I, II and III in Fig. 1: i) non-encapsulated region (I) as a reference; ii) through the WS_2 crystal (II), where the charge/spin current is injected from a ferromagnet C3 on top of the TMD crystal in to graphene and is detected in graphene, iii) across the encapsulated region ($\sim$ 3 μm) (III), where a charge/spin current is injected in graphene on one side of the TMD via contact C2 and is detected on the other side via contact C4.

All the measurements are performed using a cryostat in vacuum ($\sim 1 \times 10^{-7}$ mbar) at different temperatures between 4K and 297K. The graphene resistivity was characterized via lock-in detection (f=27.7 Hz) using a four probe method by applying a current between contacts C2-C2´and measuring a voltage drop between C1-C1´, in order to eliminate the effect of the contacts. The graphene sheet resistance ($R_{\rm sq}$) for the non-encapsulated region (region I) is $\sim$ 400 Ω (charge carrier density $\sim 10^{13} cm^{-2}$ [33] where) i.e. three times lower than for region III ($\sim$ 1.2 kΩ), indicating that graphene is less doped underneath the WS_2 crystal. The contact resistances for the FM electrodes were characterized using a three probe connection scheme, where an ac current is applied between contacts C1-C2 and a voltage drop is measured between C1-C2´. For the FM contacts on graphene, we measure a very low contact resistance ($R_{\rm C}^{\rm FM} \sim$ 200 Ω), putting our contacts in the so called conductivity mismatched regime where the contacts influence the spin transport properties of graphene [32]. Since we also fabricate the contacts on the WS_2 flake out side the WS_2-graphene interface (i.e. contacts C6-C7 on WS_2 in Fig. 1), the channel resistance ($R_{\rm sq}^{WS_2} \sim$ 70 kΩ) and the contact resistance of the FM electrodes on the WS_2 flake ($\sim$ 2-3 kΩ) can be characterized independently. The I-V behavior of the FM contacts, both on graphene and on WS_2 is characterized independently using a Keithley 2410 dc source meter. The measured I-V behavior has a linear dependence within the applied current limit (up to 40 μA), implying the presence of pin-holes (ohmic behavior) at the graphene(WS_2)-oxide interface. However, we measure a non-linear I-V behavior across the graphene-TMD interface via FM contacts (Fig. 4(a)). The observed non-linearity can be easily attributed to the presence of a potential energy barrier present only at the Gr-WS_2 interface [26, 30, 34].

Spin transport is measured in a four probe non-local detection scheme i.e. in region I, by applying a current between contacts C1 and C2´and measuring the voltage associated with the spin-accumulation between contacts C2-C5. This method decouples the paths of the spin and charge transport and thus minimizes the contribution of the charge signal to the measured spin signal [35]. For the spin valve measurements, we first apply an in-plane high magnetic field ($B_{\parallel}$) along the easy axes of the ferromagnets to align their relative magnetization. Then, the magnetic field is swept in the opposite direction to reverse the magnetization of the ferromagnets selectively based on their coercivity. We measure a sharp transition in the non-local signal ($R_{\rm NL} = V_{\rm NL}/I_{\rm ac}$) when the individual electrodes switch their magnetization direction (Fig. 2(a)). For the Hanle precession measurements, an out of plane magnetic field ($B_{\perp}$) is applied to precess the injected spins around the applied field for a fixed magnetization configuration of the ferromagnetic electrodes. While diffusing the spins precess around the applied magnetic field and dephase, showing a decrease in the magnitude of measured spin accumulation for higher fields.

Hanle precession measurements for region I, II and III are shown in Fig. 2 and Fig. 3, respectively. With these measurements, we fit the Hanle signal $\triangle R_{\rm NL} = (R_{\rm P} - R_{\rm AP})/2$, where $R_{\rm P(AP)}$ is the Hanle signal mea-

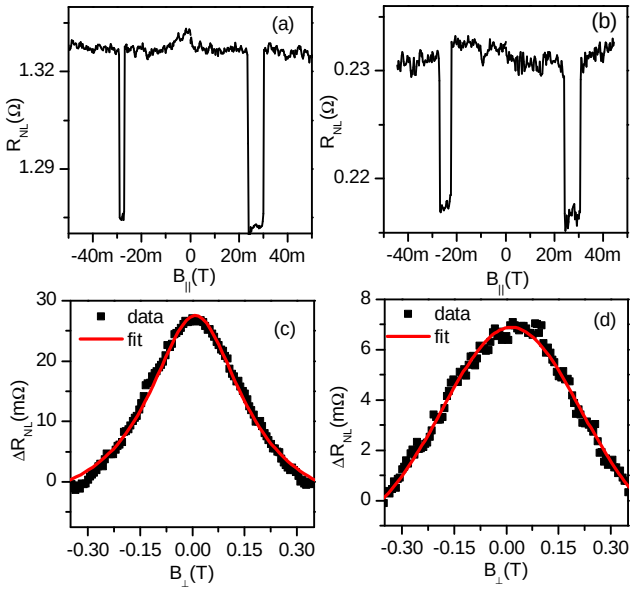

FIG. 2. (a) Spin-valve and (c) Hanle precession measurements for non-encapsulated part (region I), with the FM contacts used for spin transport. (b) spin-valve and (d) Hanle measurements for region II, where WS_2, inserted between FM contacts and graphene is used as spin-injector and the FM contact on graphene is used for measuring the spin accumulation.

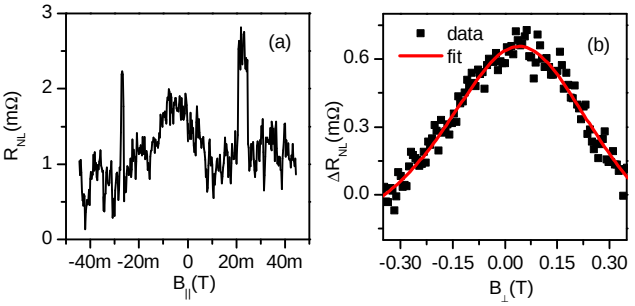

FIG. 3. (a) Spin valve and (b) Hanle measurement for the encapsulated part (region III), where a spin current is injected via a FM contact C2 (Fig. 1) on one side of the WS_2 crystal and is measured via contact C4 on the other side after traveling underneath the WS_2 environment.

sured for the parallel (anti-parallel) magnetization of the the injector-detector pair. We extract the spin diffusion coefficient D_s and spin relaxation time τ_s, following the procedure described in ref. [35] and use them to calculate the contact polarization (P). For region I, we obtain D_s ~0.09 m^2/s, $\tau_s \sim 40$ ps and $P \sim 2.3\%$, for region II, $D_s \sim 0.09$ m^2/s, $\tau_s \sim 17$ ps and $P \sim 2.7\%$ and for region III, we observe a $D_s \sim 0.1$-0.5 m^2/s, $\tau_s \sim 18$ ps and $P \sim 0.3\%$. For region III, the D_s value obtained via Hanle fitting, is sensitive to the selection of the spin-independent background, which cannot be uniquely determined here. However, we consistently obtain a reduced τ_s for region III $\sim$ 17 ps-20 ps. In conclusion, a reduced $\tau_s \leq 20$ ps is obtained via Hanle measurements for both region II and III where the spin-transport occurs underneath the WS_2 flake. Here, we would like to emphasize that a low τ_s observed in region I is probably due to the contact induced spin relaxation. For a lower contact resistance the spins can easily flow back to the contact and get relaxed, and one would obtain a lower τ_s. The actual value for τ_s can be estimated by following the procedure as described by Maassen *et al.* [32]. In this method, the effect of the contact induced spin relaxation can be quantified via `R´parameter ($R = R_c\lambda_s/R_s$), which is a ratio of the contact resistance R_c to the spin resistance (R_s) of the transport channel i.e. $R_s = R_{sq}\lambda_s/W$. Here λ_s is the spin relaxation length in graphene, and W is the width of the graphene flake. Based on this method, the actual τ_s will be three times higher than the fitted τ_s for the non-encapsulated region. For region II and III, the correction factor is $\sim$ 1, implying that the τ_s obtained via Hanle fitting procedure represents the true spin relaxation time, confirming that the spin transport is affected significantly underneath the high spin-orbit coupled material i.e. WS_2 in our case.

In order to determine the nature of charge and spin transport through the Gr-WS_2 interface, we characterize the interface resistance as a function of applied bias and temperature (Fig. 4(a)). There is an increase in the zero bias interface resistance from 80 kΩ -500 kΩ from RT to 4K. A non-linear current-voltage characteristics of the Gr-WS_2 heterostructure indicates a potential energy barrier formation at the interface. We analyze the interface I-V characteristics with the standard Schottky-Mott model at higher bias ($V_{DS} > 3k_BT/e$), which is described by the following equation:

$$I_{DS} = AA^*T^2 \exp\frac{eV_{DS}}{nk_BT} \exp\frac{-e\phi_B}{k_BT} \qquad (1)$$

where I_{DS} is the current flowing through Gr-WS_2 interface, A is the area of the interface, V_{DS} is the voltage drop across the interface, n is the ideality factor (n=1, for ideal Schottky diode), A^* is the Richardson constant, ϕ_B is the effective Schottky barrier height at the Gr-WS_2 interface, e is the electronic charge, k_B is the Boltzmann constant and T is the temperature of the device. We extract the ideality factor n and the saturation current $I_0 = AA^*T^2 \exp\frac{-e\phi_B}{k_BT}$ for different temperatures from the slope and the intercept of $\ln(I_{DS})$-V_{DS} curve of Eq. 1. The ideality factor n is highly temperature dependent (≥ 3), exhibiting a strong deviation from thermionic emission theory at lower temperatures. In Fig. 4(d), ln (I_0/T^2) versus 1000/T plot shows a positive slope for the major temperature range and the slope is only negative for very high temperatures, indicating that the elec-

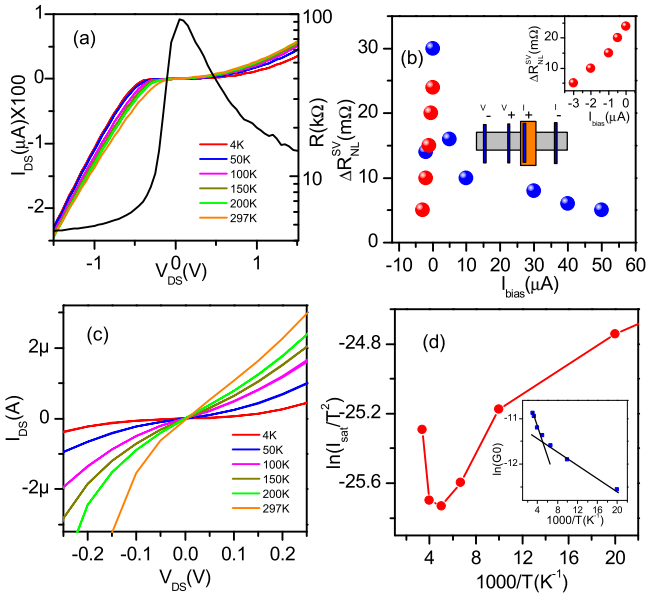

FIG. 4. (a) 2-probe I-V measurements for the graphene-WS_2 interface at different temperatures. Here WS_2 is the positive electrode. On the right y-axis, the interface resistance (dV_{DS}/dI_{DS}) is plotted as a function of V_{DS} for room temperature shows a non-linear behavior. (b) A plot of non-local spin signal ($\triangle R_{NL}^{SV} = R_P - R_{AP}$) as a function of dc bias current, injected through WS_2. The measurement scheme is shown in the cartoon. The current is applied between contacts C3-C5 of Fig. 1 and a voltage is measured between contacts C2-C2´. The spin signal is significantly reduced for a lower interface resistance. A zoomed in version for the negative I_{bias}-spin signal dependence is shown in the inset. (c) Zoomed in $I_{DS}-V_{DS}$ plot around zero bias shows more symmetric behavior, suggesting the dominance of tunnel transport over thermionic emission. (d) ln (I_{DS}) versus 1000/T plot shows a cross-over temperature (T_{cross}) around 250K from negative to positive slope, which is a signature of cross over from thermionic emission to thermal assisted tunneling in a broad temperature range. In the inset, the slope of logarithmic conductance changes around the same T_{cross}, implying the same cross-over of conduction mechanisms.

tron transport mechanism in our sample is dominated by thermally assisted tunneling or field assisted tunneling, not by the thermionic emission. We also try to fit the zero-bias conductance-temperature dependence (inset Fig. 4 (d)) with the tunnel transport model, described in ref.[34]. A plot of temperature-zero-bias conductivity shows the crossover of the two mechanisms around 200 K around the same temperature as reported in the ref. [15]. However, a reasonable agreement between the data and the fit is not obtained, possibly because of the moderate temperature dependence of the conductivity at the lower temperature. All the presented analyses support temperature assisted tunneling as a dominant charge transport mechanism across the Gr-WS_2 interface.

Novelty of the Gr-WS_2 interface is its bias dependent resistance, which in combination with the FM contact can be used to modify the conductivity mismatch condition for the spin injection. Since the charge transport across the interface is dominated by temperature assisted tunneling, it is possible to inject spins in to graphene through TMD due to small Schottky barrier and low depletion width at the interface, in contrast to the case of Si spin-valves, where no spin transport is measured due to a higher Schottky barrier at the ferromagnet-silicon interface of the injector and the detector electrodes [36, 37]. In order to bias the interface, we use a dc current source at different currents with a fixed small ac current (0.5 μA) superimposed on it. The spin accumulation is measured non-locally via the lock-in detection. On changing the bias current, the interface resistance is modulated from 15 kΩ -100 kΩ for the positive current bias and to 4 kΩ for the negative bias. The change in the resistance is much sharper for the negative bias regime. The spin signal decreases slowly from 50 mΩ-to 5 mΩ for the positive current range of 50 μA. For the negative bias, we observe similar change in within 5 μA current range, suggesting a strong correlation between the interface resistance and spin injection efficiency. However, for the oxide tunnel barriers with 4 kΩ interface resistance, one can get a reasonable spin injection, as this situation is not a poor conductivity mismatch. Even for smaller interface resistance in region I, we were able to achieve spin injection. A negligible spin injection for a reasonable interface resistance, suggests towards either low spin polarization of the interface as it is not a pure tunneling or additional spin-relaxation underneath the WS_2 encapsulated region. Also, we were unable to detect any spin accumulation on the other side of WS_2 (contact C4), probably due to the combined effect of poor spin injection through the TMD, accompanied by relatively long distance experienced by spins underneath WS_2, before getting detected. However, from the present measurements, we cannot comment on the the source of enhanced spin relaxation process.

In conclusion, we demonstrate that spin transport across the WS_2 encapsulated region and the spin transport is reduced in the proximity of the TMD crystal. At present, we cannot comment on the source of additional spin-relaxation whether it is caused by proximity induced spin orbit coupling or due to spin absorption via the TMD. We also demonstrate the use of WS_2 as a bias dependent spin injector due to the non-linear charge transport properties of Gr-WS_2 interface. Via a temperature-dependent charge transport analysis, we find out that the dominating charge transport mechanism across the interface is thermally assisted tunneling, which helps the spins to tunnel through the Schottky barrier.

We acknowledge J. G. Holstein, H. M. de Roosz and H. Adema for their technical assistance. This research work was financed under EU-graphene flagship program

(637100) and supported by the Zernike Institute for Advanced Materials and the Netherlands Organization for Scientific Research (NWO).

* corresponding author; s.omar@rug.nl

[1] C. Ertler, S. Konschuh, M. Gmitra, and J. Fabian, Phys. Rev. B **80**, 041405 (2009).

[2] D. Huertas-Hernando, F. Guinea, and A. Brataas, Phys. Rev. Lett. **103**, 146801 (2009).

[3] P. J. Zomer, M. H. D. Guimarães, N. Tombros, and B. J. van Wees, Phys. Rev. B **86**, 161416 (2012).

[4] J. Ingla-Aynés, M. H. D. Guimarães, R. J. Meijerink, P. J. Zomer, and B. J. van Wees, Phys. Rev. B **92**, 201410 (2015).

[5] S. Datta and B. Das, Appl. Phys. Lett. **56**, 665 (1990).

[6] G. R. Bhimanapati, Z. Lin, V. Meunier, Y. Jung, J. Cha, S. Das, D. Xiao, Y. Son, M. S. Strano, V. R. Cooper, L. Liang, S. G. Louie, E. Ringe, W. Zhou, S. S. Kim, R. R. Naik, B. G. Sumpter, H. Terrones, F. Xia, Y. Wang, J. Zhu, D. Akinwande, N. Alem, J. A. Schuller, R. E. Schaak, M. Terrones, and J. A. Robinson, ACS Nano **9**, 11509 (2015).

[7] H. Jiang, J. Phys. Chem. C **116**, 7664 (2012).

[8] X. Xu, W. Yao, D. Xiao, and T. F. Heinz, Nat Phys **10**, 343 (2014).

[9] Z. Y. Zhu, Y. C. Cheng, and U. Schwingenschlögl, Phys. Rev. B **84**, 153402 (2011).

[10] D. W. Latzke, W. Zhang, A. Suslu, T.-R. Chang, H. Lin, H.-T. Jeng, S. Tongay, J. Wu, A. Bansil, and A. Lanzara, Phys. Rev. B **91**, 235202 (2015).

[11] L. Bawden, S. P. Cooil, F. Mazzola, J. M. Riley, L. J. Collins-McIntyre, V. Sunko, K. W. B. Hunvik, M. Leandersson, C. M. Polley, T. Balasubramanian, T. K. Kim, M. Hoesch, J. W. Wells, G. Balakrishnan, M. S. Bahramy, and P. D. C. King, Nat Commun **7**, 11711 (2016).

[12] W. Yao, D. Xiao, and Q. Niu, Phys. Rev. B **77**, 235406 (2008).

[13] Q. H. Wang, K. Kalantar-Zadeh, A. Kis, J. N. Coleman, and M. S. Strano, Nat Nano **7**, 699 (2012).

[14] W. J. Yu, Z. Li, H. Zhou, Y. Chen, Y. Wang, Y. Huang, and X. Duan, Nat Mater **12**, 246 (2013).

[15] T. Georgiou, R. Jalil, B. D. Belle, L. Britnell, R. V. Gorbachev, S. V. Morozov, Y.-J. Kim, A. Gholinia, S. J. Haigh, O. Makarovsky, L. Eaves, L. A. Ponomarenko, A. K. Geim, K. S. Novoselov, and A. Mishchenko, Nat Nano **8**, 100 (2013).

[16] N. Myoung, K. Seo, S. J. Lee, and G. Ihm, ACS Nano **7**, 7021 (2013).

[17] Y.-F. Lin, W. Li, S.-L. Li, Y. Xu, A. Aparecido-Ferreira, K. Komatsu, H. Sun, S. Nakaharai, and K. Tsukagoshi, Nanoscale **6**, 795 (2013).

[18] M. Gurram, S. Omar, S. Zihlmann, P. Makk, C. Schönenberger, and B. J. van Wees, Phys. Rev. B **93**, 115441 (2016).

[19] M. V. Kamalakar, A. Dankert, J. Bergsten, T. Ive, and S. P. Dash, Sci. Rep. **4**, 6146 (2014).

[20] C. A. Joiner, P. M. Campbell, A. A. Tarasov, B. R. Beatty, C. J. Perini, M.-Y. Tsai, W. J. Ready, and E. M. Vogel, ACS Appl. Mater. Interfaces **8**, 8702 (2016).

[21] P. Goswami, arXiv:1606.02413 [cond-mat] (2016), arXiv: 1606.02413.

[22] A. Avsar, J. Y. Tan, T. Taychatanapat, J. Balakrishnan, G. K. W. Koon, Y. Yeo, J. Lahiri, A. Carvalho, A. S. Rodin, E. C. T. O'Farrell, G. Eda, A. H. Castro Neto, and B. Özyilmaz, Nat Commun **5**, 4875 (2014).

[23] P. Wei, S. Lee, F. Lemaitre, L. Pinel, D. Cutaia, W. Cha, F. Katmis, Y. Zhu, D. Heiman, J. Hone, J. S. Moodera, and C.-T. Chen, Nat. Mater. **15**, 711 (2016).

[24] W. Yang, J. Shang, J. Wang, X. Shen, B. Cao, N. Peimyoo, C. Zou, Y. Chen, Y. Wang, C. Cong, W. Huang, and T. Yu, Nano Lett. **16**, 1560 (2016).

[25] Z. Wang, D.-K. Ki, J. Y. Khoo, D. Mauro, H. Berger, L. S. Levitov, and A. F. Morpurgo, arXiv:1606.01789 [cond-mat] (2016), arXiv: 1606.01789.

[26] J. Tian, T.-F. Chung, I. Miotkowski, and Y. P. Chen, arXiv:1607.02651 [cond-mat] (2016), arXiv: 1607.02651.

[27] Z. Wang, D.-K. Ki, H. Chen, H. Berger, A. H. MacDonald, and A. F. Morpurgo, Nat Commun **6**, 8339 (2015).

[28] E. C. T. ÕFarrell, A. Avsar, J. Y. Tan, G. Eda, and B. Özyilmaz, Nano Letters **15**, 5682 (2015).

[29] P. J. Zomer, M. H. D. Guimarães, J. C. Brant, N. Tombros, and B. J. v. Wees, Appl. Phys. Lett. **105**, 013101 (2014).

[30] R. Moriya, T. Yamaguchi, Y. Inoue, S. Morikawa, Y. Sata, S. Masubuchi, and T. Machida, Appl. Phys. Lett. **105**, 083119 (2014).

[31] B. Yang, M.-F. Tu, J. Kim, Y. Wu, H. Wang, J. Alicea, R. Wu, M. Bockrath, and J. Shi, 2D Mater. **3**, 031012 (2016).

[32] T. Maassen, I. J. Vera-Marun, M. H. D. Guimarães, and B. J. van Wees, Phys. Rev. B **86**, 235408 (2012).

[33] Since we do not have a working back gate for the reported sample, we estimate the carrier density n from the relation $n = 1/R_{\rm sq}e\mu$, where e is the electron charge and μ is the field effect mobility. Here, we take $\mu \sim 5000\ cm^2V^{-1}s^{-1}$ which is usually obtained for good quality graphene samples on SiO_2 substrate.

[34] T. Yamaguchi, R. Moriya, Y. Inoue, S. Morikawa, S. Masubuchi, K. Watanabe, T. Taniguchi, and T. Machida, Appl. Phys. Lett. **105**, 223109 (2014).

[35] N. Tombros, C. Jõzsa, M. Popinciuc, H. T. Jonkman, and B. J. van Wees, Nature **448**, 571 (2007).

[36] R. Jansen and B. C. Min, Phys. Rev. Lett. **99**, 246604 (2007).

[37] R. Jansen, B. C. Min, S. P. Dash, S. Sharma, G. Kioseoglou, A. T. Hanbicki, O. M. J. van 't Erve, P. E. Thompson, and B. T. Jonker, Phys. Rev. B **82**, 241305 (2010).

Supplementary Information

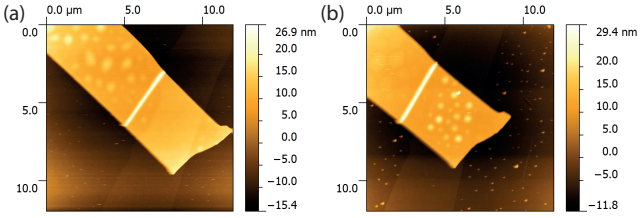

FIG. S1. A graphene-WS_2 stack (a) before annealing and after (b) annealing. For the thin WS_2 flakes ($t_{WS_2} \sim 5$nm), the graphene flake underneath the WS_2 flake can be seen through. Here, the annealing step does not seem to improve the interface quality significantly.

Due to the layered structure of graphene and WS_2, these materials can be exfoliated via a scotch-tape method. The graphene flake is exfoliated from a bulk HOPG (highly oriented pyrolytic graphite) ZYA grade crystal (supplier: SPI) on to a pre-cleaned Si-SiO_2 substrate (t_{SiO_2}=300 nm). A single layer is identified via an optical microscope. A WS_2 flake (spplier: HQ Graphene) is exfoliated on a vsicoelastic PDMS (polydimethylsiloxane) substrate. The freshly cleaved WS_2 flake on the PDMS is brought in contact with the graphene flake in a transfer stage. Since the adhesion of WS_2 on the PDMS stamp is relatively weak compared to the GrW van der Waals interaction and the SiO_2-WS_2 adhesion, the flake is easily stacked on to the desired graphene flake. As a result a smooth interface is formed, which is identified with an atomic force microscope (AFM). For a thick WS_2 flake the bubble formation during the transfer procedure is less likely and in the AFM we do not observe any bubbles at the graphene-WS_2 interface. The prepared stacks are annealed at 250°C for 5 hours in an Ar-H_2 environment for removing the residue polymers. However, for most of the stacks, we only observe that the uncovered graphene and WS_2 flake looks more clean after the annealing steps, leaving the graphene-WS_2 interface more or less similar to that before the annealing (Fig. S1).

For the stack with a thick $WS_2 \sim 20$ nm flake, transferred on to a graphene flake, we do not see a bubble formation at the graphene-WS_2 interface (Fig. S2). Still the furnace annealing is performed to clean the polymer residues from the uncovered surfaces.

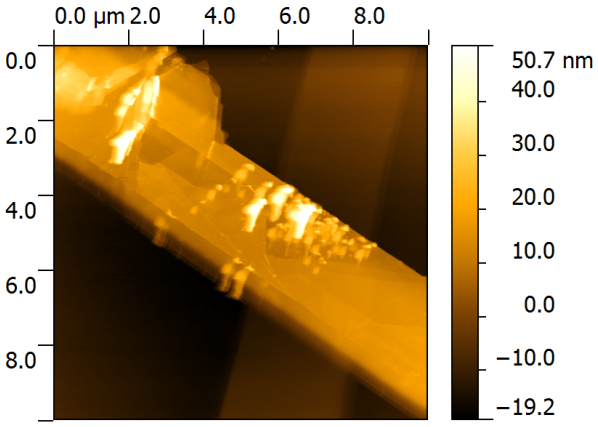

FIG. S2. A graphene-WS_2 stack formed with thick WS_2 flakes ($t_{WS_2} \sim 20$nm)